Localization, confinement, and field-controlled propagation of spin waves in Ni$_{80}$Fe$_{20}$ antidot lattices

Sebastian Neusser, Bernhard Botters, and Dirk Grundler[*]

Department E10, Fakultät für Physik, TU München, James-Franck-Strasse 1, 85747 Garching, Germany
(Received 7 March 2008; revised manuscript received 29 May 2008; published 6 August 2008)

Spin-wave modes in Ni$_{80}$Fe$_{20}$ thin-film antidot lattices are investigated using micromagnetic simulations and a semianalytical theoretical approach. The simulations reveal a rich eigenmode spectrum consisting of edge and center modes. We find both spatially localized and spin waves extending over many unit cells. To classify the different types of modes and to analyze the microscopic properties, we adapt a semianalytical approach. We show how to reduce the two-dimensional problem of the antidot lattice to a one-dimensional problem if certain high-symmetry axes are considered. For lattices of unit-cell lengths ranging from 200 to 1100 nm, we find that the characteristic mode eigenfrequencies can be correlated with both local inhomogeneities of the demagnetization field and specific wave vectors caused by geometry-imposed mode quantization conditions. We compare our results with recently published experimental data and discuss the crossover from dipolar to exchange-dominated spin waves. Moreover, we simulate propagation of spin waves and find a preferred axis of propagation perpendicular to the external magnetic field.

I. INTRODUCTION

Recent investigations on quantized spin-wave modes in individual mesoscopic magnets[1] and propagation in individual magnon wave guides[2] have substantiated the idea of magnonics.[3] This emerging research field addresses the transmission, logical modification, and storage of information using spin waves.[2,4–7] Here, mesoscopic antidot lattices, i.e., thin ferromagnetic films such as permalloy Ni$_{80}$Fe$_{20}$, Co, etc., which are periodically structured with holes, are in particular interesting. They form a periodic array of microscopic magnets *interconnected* via magnetic nanowires, i.e., magnon wave guides. Two different viewpoints have been put on a magnetic antidot lattice so far: On the one hand, starting from the perspective of a magnetic memory device, antidot lattices have gained considerable interest. They exhibit pronounced hysteresis effects, which might serve for high-density data storage.[8–10] To investigate spin-wave excitations within such lattices, different techniques have been applied: cavity ferromagnetic resonance (FMR),[11–13] Brillouin light scattering,[14,15] and spatio-temporal magneto-optical Kerr effect (MOKE).[16] In Ref. 11 Yu *et al.* have reported that spin-wave modes in antidot lattices depend on the lattice geometry and that, besides a so-called edge mode, two further major resonances occur (cf. Fig. 4 in Ref. 12). Pechan *et al.*[16] were able to directly measure the spatial mode profiles of these two modes. They analyzed them in terms of uniform spin precession. They assumed a standing spin wave with wave vector $k=0$ and fitted the demagnetization field to find the eigenfrequency. A comparable approach was used by McPhail *et al.*[14] Hole diameters in the cited experiments varied from 300 nm in Ref. 15 to, e.g., 1500 nm in Ref. 16; however, to our knowledge, a discussion of the influence of lattice size on spin-wave eigenfrequencies has not been given so far. On the other hand, starting from the physics of a photonic crystal,[17] periodic holes in a magnetic film are expected to modify the transmission of spin waves with wave vectors $k \neq 0$. Due to challenges in nanopatterning and effi-

cient detection schemes, experiments in this field are only few so far. In Ref. 18 the authors measured the transmission of *propagating* Damon-Eshbach-type spin waves through an antidot lattice and found an absorption band that they explained by Bragg-type reflection. However, *standing* spin waves might also affect the transmission due to excitation and resonant absorption at characteristic eigenfrequencies. Bragg-type reflection and resonant absorption thus need to be distinguished. Orthodox theories would suggest excitation of eigenmodes with a wave vector k being a multiple of a reciprocal lattice vector $2\pi/a$, where a is the lateral lattice constant.[19] We will show however that this approach is not valid for magnetic antidot lattices. In contrast to, e.g., photonic crystals, where the geometric edges determine the boundary conditions, the inhomogeneity of the internal magnetic field H_{int} is found to impose further *intrinsic* boundary conditions for spin-wave modes. Within a magnetic material the wave vector and group velocity of spin waves become position dependent due to H_{int}. A possible analogy in a photonic crystal would be a smooth variation of the refractive index of the dielectric. It is in particular interesting to separate modes from each other which are either localized in an extremum of H_{int},[20] i.e., are confined within a particular unit cell, or extend around holes[21] and spread throughout the lattice. We call the latter modes extended. Furthermore, the orientation of $\vec{k}$ with respect to magnetization $\vec{M}$ varies the kind of spin wave, from, e.g., a Damon-Eshbach-type mode $(\vec{k} \perp \vec{M})$ to a backward volume mode $(\vec{k} \| \vec{M})$. All these features outlined above make magnetic antidot lattices in particular intriguing for studying wave phenomena. A detailed understanding of the spin-wave eigenmodes is essential for further developments in magnonics.

In this paper we investigate spin-wave modes in nanostructured permalloy antidot lattices subject to an applied external field H. Our results highlight the twofold influence of the periodic arrangement of holes: they change the internal demagnetization fields and impose characteristic quantization conditions. The geometry confines spin waves with

quantized wave vectors $k \neq 0$ in contrast to assumptions in the earlier publications.[14,16] At the same time the inhomogeneous internal field tends to localize specific modes in distinct lattice areas. Prominent extended modes are found in the interconnecting nanowires which are transversely magnetized. We use a semianalytical approach following Refs. 22 and 23 to interpret the micromagnetic simulation results in detail.

The paper is organized as follows: In Sec. II we introduce a semianalytical approach, allowing investigation of the nature of a particular spin-wave mode and adapt it accordingly to treat the two-dimensional (2D) problem of an antidot lattice. In Sec. III we apply this theory to results of a set of micromagnetic simulations of antidot lattices and use it to explain the methodology of observed *standing* spin waves. In Sec. IV we discuss the influence of both wave-vector confinement and demagnetization field on the spin-wave eigenfrequency for various lattice sizes and identify the two respective regimes. Finally, in Sec. V, using simulation analysis in time domain, we show how spin waves *propagating* parallel and perpendicular to the external field in an antidot lattice are differently affected by the internal magnetic field.

II. THEORY

To analyze spin excitations in antidot lattices (cf. Fig. 1) prepared from ferromagnetic material, we have performed both micromagnetic simulations and a semianalytical approach. The semianalytical approach will be powerful to classify the different modes found both in the simulations and in earlier experiments.[16] The classification is important to figure out antidot lattice modes, which are characteristic and vary systematically as a function of lattice constants, lattice geometries (cf. Table I), and external magnetic field H. In particular, H is known to induce transitions between different quasistatic magnetization configurations.[9] Resonances detected, e.g., via FMR, might therefore originate from different domain configurations as already observed on individual micromagnets.[23] The applied external field also varies the inhomogeneity of the internal field and thereby changes conditions for the excitation of spin wave with $k \neq 0$ in the FMR experiment. As a consequence characteristic modes might exist only between upper and lower critical fields.[21] Field-dependent investigations, as depicted in Fig. 2, are therefore important. Based on such data, a stringent classification of spin waves can be developed in order to understand excitations in topologically complex devices such as antidot lattices.

Since we deal with a nanopatterned film of permalloy, which is thin if compared to the relevant lateral widths, we assume in the following that spin excitations in growth direction, i.e., z direction, are uniform. We can thereby reduce the three-dimensional topological problem to the two lateral directions x and y (see Fig. 1). The finite film thickness only enters the exact spin-wave eigenfrequency. Here it is important to note that in two dimensions, still it is not possible *a priori* to apply the semianalytical approach reported by Guslienko *et al.* in Ref. 22. In an antidot lattice, mode profiles
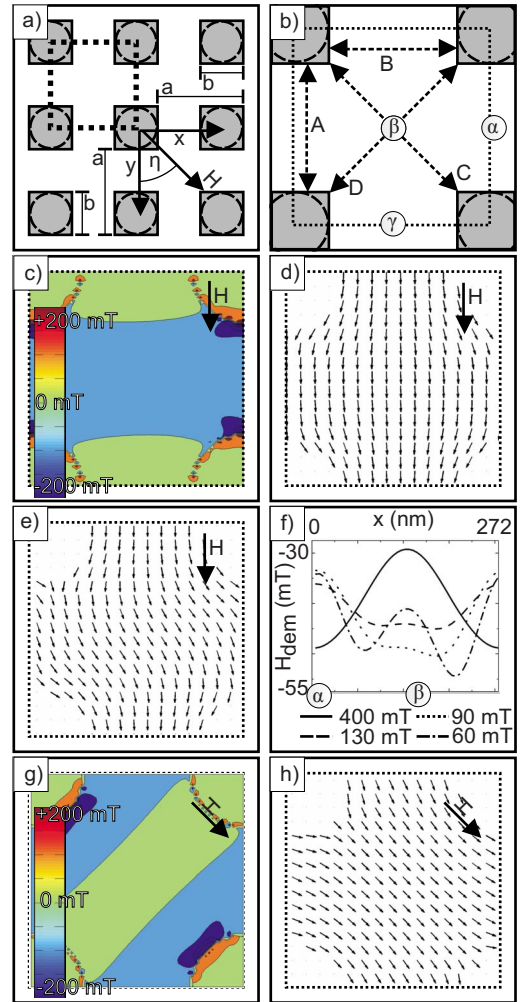

FIG. 1. (Color online) (a) Sketch of an antidot lattice where we define lateral parameters. Dark gray represents holes. We investigate holes of both square shape (full line) and circular shape (dashed line). (b) The square shown as a dotted line depicts the unit cell for the simulations. Relevant lattice directions A to D and specific areas α, β, and γ are indicated. (c)–(h) show the static behavior of lattice 3, with a lateral unit cell size of 272 nm. In particular: (c) Demagnetization field H_{Dem} in the butterfly state [cf. (d)] at 100 mT (color code: see legend). Magnetization configuration: (d) the butterfly state at 100 mT ($\eta = 0°$) and (e) waterfall state at 30 mT ($\eta = 0°$). Small arrows indicate local orientation of spins. (f) Internal field profile through areas α and β in the x direction at $y = a/2$. For smaller fields the butterfly state gets more pronounced. (g) Demagnetization field H_{Dem} and (h) magnetization configuration for $\eta = 45°$ and $\mu_0 H = 100$ mT. Dynamic demagnetization field changes as simulated (see Sec. III A) are less than 0.1 mT.

cannot be separated straightforwardly in components parallel and orthogonal to the magnetization. This is due to first an inhomogeneous demagnetization field $\vec{H}_{\mathrm{Dem}}$ in the x *and* y direction, as well as second due to the inhomogeneous internal field $\vec{H}_{\mathrm{int}}(x, y)$, which locally points in different directions. We have found, however, that in antidot lattices for distinct areas and specific modes, we are able to reduce the 2D problem to an effective one-dimensional (1D) problem if one component of the wave vector is known or can be

TABLE I. Parameters of antidot lattices

Lattice	Unit cell size (nm)	Hole diameter (nm)	Hole shape	Hole area/unit cell area (%)	Thickness (nm)
1	206×206	85	square	17.4	24
2	272×272	85	square	9.8	24
3	272×272	136	circular	19.6	24
4	1100×1100	550	square	25	16

guessed reasonably well from the lattice geometry. This is in particular true if a high-symmetry direction is considered. Once we know one component of the total in-plane wave vector $\kappa^2 = k_\perp^2 + k_\parallel^2$ (from the lattice symmetry directly or a micromagnetic simulation), we conduct semianalytical cal-
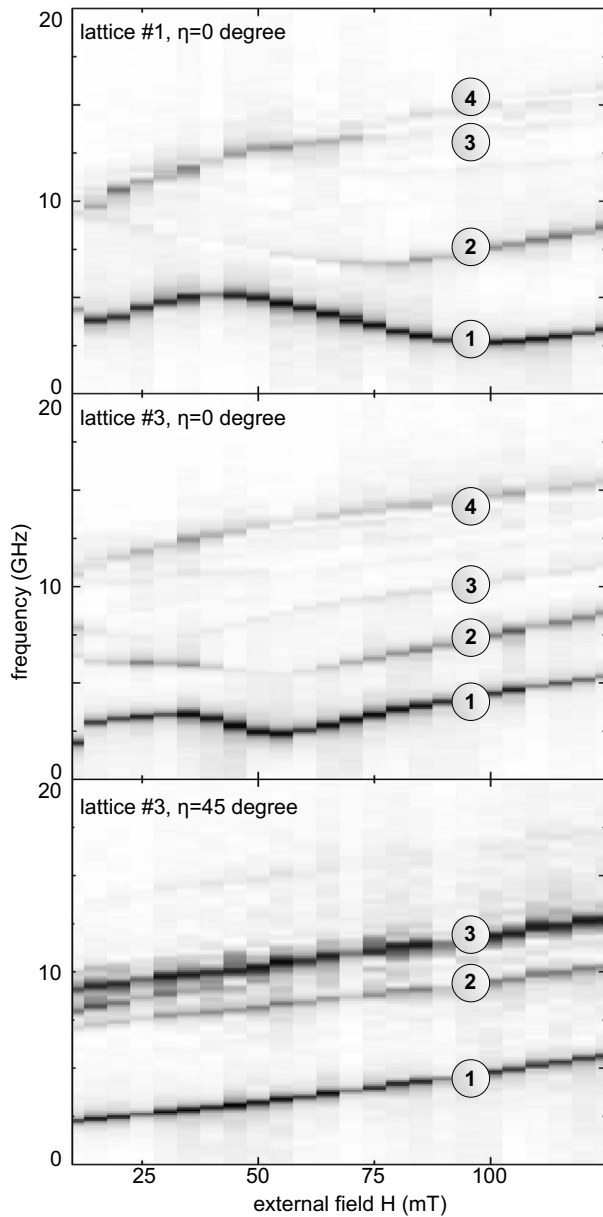

FIG. 2. Simulated magnetic field dispersions for (a) lattice 1 at $\eta = 0°$, (b) lattice 3 at $\eta = 0°$, and (c) lattice 3 at $\eta = 45°$.

culations and consistency checks following the methods of Ref. 23. Introducing the wave vector component $k_\perp$ ($k_\parallel$), which is perpendicular (parallel) to a *high-symmetry direction parallel to H*, has turned out to be powerful in order to classify characteristics of antidot lattice modes and to shed light on the microscopic properties.

In detail, we have performed the following calculation steps: we start from time-dependent micromagnetic simulations.[24] We uniformly excite frequencies in the giga-hertz range and address the linear spin-dynamics regime.[25] For simulation parameters see Sec. III A. Spatially and frequency-resolved Fourier transform imaging[26] is performed at the resonance frequency of a distinct mode to il-lustrate its spatial characteristics (Fig. 3). We have found that once the frequency and spatial distributions of a spin-wave mode are known, symmetry axes of the antidot lattice allow us to guess reasonably well one of the relevant wave-vector components, i.e., either the wave vector perpendicular $k_{n\perp}$ or parallel $k_{m\parallel}$ to the external field. The parameters n, m count the number of nodes in respective orthogonal directions, i.e., for the perpendicular case $k_{n\perp} = (n+1)\pi/w_\perp$, where $w_\perp$ is the respective quantization width. Anticipation of the wave vector can be achieved by, e.g., measuring the localization distance and the node number in the spatial Fourier trans-form images of the mode and by this means recalculating the wavelength and wave vector. The wave vector is estimated best first, if geometry itself and/or simulated mode profile allow a clear identification of the wave vector and second, if H_{Dem} is varying slowly along the axis along which the wave vector is anticipated. For arbitrary directions within the anti-dot lattice, i.e., not along a high-symmetry axis, the wave vector will vary in orientation and magnitude within a unit cell. Then two components of the wave vector change sig-nificantly and our semianalytical approach cannot be per-formed. Furthermore, we have treated the studied modes as having a vanishing local-magnetization contribution perpen-dicular to the applied field. This treatment has turned out to be a very good approximation. Now, to classify in detail the nature of the different antidot lattice modes and to extract characteristic spin-wave phenomena, we follow the semiana-lytical approach using the dispersion relation[22]

$$\omega_{mn}^2 = (\omega_H^{mn} + \alpha\omega_M \kappa_{mn}^2)\{\omega_H^{mn} + \omega_M \cdot [\alpha\kappa_{mn}^2 + F_{mn}(\kappa_{mn})]\},$$
(1)

where $\kappa_{mn}^2 = k_{n\perp}^2 + k_{m\parallel}^2$ denotes the total in-plane wave vector, ω_{mn}^2 is the frequency of the mode, $F_{mn}(\kappa_{mn})$ the dipole matrix element,[22] α the exchange constant, and $\omega_M = 4\pi\gamma M_s$, where M_s is the saturation magnetization and $\gamma/2\pi$
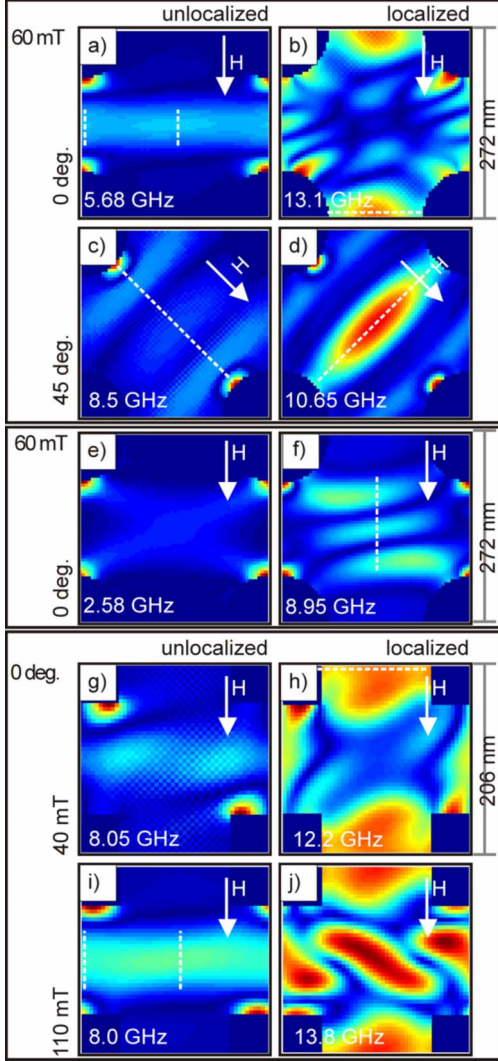
FIG. 3. (Color online) Color-coded mode profiles for lattice 3 (a)–(f) and lattice 1 (g)–(j). Red (bright) means high-precession amplitude, dark blue reflects zero amplitude. The orientation of H is indicated by the white arrow. Broken lines illustrate high-symmetry axes along which mode analysis is performed (see text). Lattice 3: eigenfrequencies at 60 mT are (a) 5.68 GHz (mode 0Deg-2), (b) 13.1 GHz (mode 0Deg-4), (c) 8.5 GHz (mode 45Deg-2), (d) 10.65 GHz (mode 45Deg-3), (e) 2.58 GHz (mode 0Deg-1, edge mode), (f) 8.95 GHz (mode 0Deg-3). Lattice 1: (g) 8.05 GHz (mode 0Deg-2 at 40 mT), (h) 12.2 GHz (mode 0Deg-4 at 40 mT), (i) 8.0 GHz (mode 0Deg-2 at 110 mT), and (j) 13.8 GHz (mode 0Deg-4 at 110 mT).

=2.95 GHz/kOe the gyromagnetic ratio. The parameter $\omega_H^{mn} = \gamma H_{int}$ is the precession frequency related to the effective internal field $H_{int} = H_{Dem} + H$. The undefined wave-vector component, either $k_{n\perp}$ or $k_{m\parallel}$, is calculated along a high-symmetry axis using Eq. (1) accordingly to yield the eigenfrequency ω_{mn} of the mode known from simulation. For this Eq. (1) is solved numerically for the free wave-vector component at each coordinate ξ along the high-symmetry axis. For values of ξ, where a nonimaginary wave vector results from the calculation, the total wave vector $\kappa(\xi)$ is then known. At this point, there are three possibilities to check the consistency of the anticipated wave vector and thus of the nature of the mode, all of which can be used independently.

First, we follow a quasiclassical (WKB) argument according to Refs. 22 and 27

$$\phi_{WKB} = \int_a^b k_{\perp,\parallel}[\omega_{mn}, H_{int}(\xi)]d\xi = (p+1)\pi, \qquad (2)$$

where ϕ_{WKB} is the phase acquired by the standing spin wave between turning points a and b along the high-symmetry axis and $p = 0, 1, 2, ... $ p is the order of the mode in the direction of the high-symmetry axis and therefore is given by $p = n$, if the high-symmetry axis is perpendicular to the field, or by $p = m$ otherwise. Equation (2) must be fulfilled to form a standing spin wave. The dependence of the free wave vector $k_{n\perp}$ or $k_{m\parallel}$ on frequency ω is given by dispersion relation Eq. (1) as discussed above. Turning points are defined by either an imaginary wave vector[22] by a vanishing internal field[1] or by geometrical edges of the holes.[11] In small structures and for small H it is not easily possible to identify turning points: in the vicinity of an antidot edge H_{Dem} is very high as compared to the external field H. It is then not possible to distinguish dipolar-dominated from exchange-dominated modes. In such a case, the simple picture of cosine and sine modes is not applicable anymore[28] and turning points are not easily found. Throughout this text we will use Eq. (2) to find out the nature of the mode. We call this procedure WKB analysis. If a value close to an integral number of π is yielded, the nature of the mode has been anticipated correctly. Within the limitations of accuracy imposed by the semianalytical approach, one expects relative errors $\lesssim 20\%$.[23,27]

Second, it is possible to assume the mode nature as a sine or cosine function,[29] i.e., symmetric or asymmetric and, using the semianalytically calculated wave vector, calculate the mode profile. In general for the sine case one gets

$$m(\xi) = \sin[\xi \cdot k_{\perp,\parallel}(\xi)]. \qquad (3)$$

This mode profile should then be compared to the simulated patterns.

Third, once the mode profile is known, an averaged demagnetization field value is calculated according to Ref. 23

$$\overline{H_{Dem}} = \frac{\sum_{x,y} H_{Dem}(x,y) \cdot m(x,y)^2}{\sum_{x,y} m(x,y)^2}, \qquad (4)$$

where $m(x,y)^2$ reflects the spatial-mode amplitude at a given coordinate omitting the phase. The summation extends over a unit cell of the antidot lattice. $H_{Dem}(x,y)$ can be taken from the simulation. Using the anticipated wave-vector component, a spatially averaged value of the previously calculated component and the averaged demagnetization field value $\overline{H_{Dem}}$, an average resonance frequency can be calculated using Eq. (1). The calculated ω_{mn} should then be compared to the simulated one. If eigenfrequencies from both approaches match, one can classify modes in different antidot lattices with respect to (i) symmetry, (ii) boundary conditions, and (iii) number of nodes. Moreover, based on the parameters outlined above, the semianalytical formalism allows us to calculate frequencies of higher-order modes directly with no further adjustable parameter. This can be done by assuming a

localization length according to the lowest-order wave vector as discussed above, and subsequently increasing the number of nodes yielding the higher-order wave vectors. These higher-order modes serve as a further and independent consistency check of respective eigenmodes extracted from simulations.

III. SPIN EXCITATIONS OF ANTIDOT LATTICES

A. Lattice parameters and quasistatic magnetization configurations

We study eigenmodes of antidot lattices with different geometrical parameters. We are interested in the impact of the shape of the hole (square vs circular), the lattice constant, and the inverse filling fraction, i.e., the ratio between the area without magnetic material and the total device area. In this work we focus on square lattices [Figs. 1(a) and 1(b)]. Table I summarizes the parameters. For lattice 4 we have considered deviations from a regular hole shape in order to simulate fabrication imperfections. From this data set (not shown) we have found that the main center modes, which we will discuss in detail below, do not show any major dependence on edge roughness. Lattices are simulated by defining a lattice unit cell [Fig. 1(b)] and using periodic boundary conditions. Hence we assume an infinite array in a coherent magnetic state. This assumption is reasonable if we compare our lattice constants of <300 nm (samples 1 to 3) and 1.1 μm (sample 4) with a spin-wave coherence length of 18 μm and beyond in permalloy.[30] Crystal anisotropy is not considered. The cell size for discretization of the magnetic material is 4.25 nm for lattices 1 to 3, 4.3 nm for lattice 4 in the x and y direction, and 4 nm in the z direction for all four lattices. The temperature is set to be 0 K, as reference simulations prove that a finite temperature does not significantly alter the results. Saturation magnetization is $\mu_0 \times M_{\mathrm{Sat}} = 1080$ mT. Exchange constant is 13×10^{-12} J/m. We excite magnetization dynamics using an in-plane pulsed excitation $\vec{h}(t)$ in the x direction of 3 ps duration and 0.12 mT amplitude. Thus the linear regime is addressed. Damping constant is set to $\alpha = 0.01$.

Simulations are performed in two different orientations of the external field H: H parallel to a square lattice axis, i.e., the angle η is $\eta = 0°$ [cf. Figs. 1(c)–1(f)], and H along a diagonal ($\eta = 45°$) [Figs. 1(g) and 1(h)]. For $\eta = 0°$ we obtain two characteristic magnetization configurations. Their occurrence depends on the exact value of H and lattice parameters. They are depicted in Figs. 1(d) and 1(e). The so-called butterfly magnetization configuration (d) is known from Ref. 13 and occurs in lattices 1 to 3 for $\mu_0 H \gtrsim 60$ mT and lattice 4 for all H. The demagnetization field shown in Fig. 1(c) reflects the symmetry of the magnetization configuration. For lattices 1 to 3 a small misalignment of $0° < \eta < 1°$ or, importantly, an excitation field $\vec{h}(t)$ perpendicular to $\vec{H}$ induce at small fields $\mu_0 H \lesssim 60$ mT a further magnetization configuration[9] depicted in Fig. 1(e). It exhibits a nonvanishing magnetization perpendicular to $\vec{H}$. In the following we will label this configuration "waterfall state," as the microscopic moments follow a waterfall-like orientation. A similar

tilt of the magnetization for small structures at small fields has been observed before in magnetic wires[31] and can be understood considering increasing field expulsion by surface charges for nanostructures. From this it is expected that the magnetization component perpendicular to $\vec{H}$ grows with smaller field and smaller structure size. This tendency is indeed observed in the simulations discussed here: the smaller the lattice and external field H, the larger is the fraction of spins tilted away from the external field direction.

In the following we will mainly discuss so-called center modes and will not focus on the modes that are localized right at the edges of the patterned holes. This has two reasons: first, edge modes localized in the spin-wave wells at the edges[1] will be influenced strongly by the shape of the hole and edge roughness. These modes might therefore vary substantially from array to array. Eigenfrequencies might even change from hole to hole in a real antidot lattice. Second, mode confinement next to a hole edge will not allow separation of the two wave vectors along a high-symmetry axis. The demagnetization field changes on a short length scale along all directions. This makes application of our semianalytical approach for edge mode analysis and classification unappropriate.[32]

B. Mode analysis

We first discuss modes that are prominent at $\eta = 0°$ for large H. We begin the analysis with the magnetic-field dispersion of eigenmodes in lattice 1 [Fig. 2(a)] and lattice 3 [Fig. 2(b)]. Dark gray color corresponds to power absorption, i.e., excitation of spin-wave modes. For $\mu_0 H \gtrsim 60$ mT we observe four prominent resonance frequencies. For the discussion we will label these modes using the angle η, an index number ranging from 1 to 4, and if useful, we will provide the number of nodes n or m in the orthogonal lateral directions.

1. Edge mode at $\eta = 0°$

Lowest in frequency is mode 0Deg-1. This mode is illustrated in Fig. 3(e). When we compare the spatially resolved MOKE images of Ref. 16 and the spatially resolved Fourier transform images obtained from simulation, mode 0Deg-1 is found to be consistent with the edge mode experimentally observed. In both images, the mode amplitude is high only in areas of very high demagnetization field bordering to the holes. The low frequency reflects the small value of the internal field near the edges due to the large and negative demagnetization field [dark blue color in Fig. 1(c)]. We will not discuss this edge mode in detail for reasons explained above.[33]

2. Extended mode at $\eta = 0°$

Next, we consider mode 0Deg-2 [Figs. 3(a) and 3(i)]. This type of mode resides in the magnetic nanowires, which run perpendicular to the external field. It extends in horizontal direction from the left to the right end of the lattice. This mode closely remodels a further mode experimentally observed in Ref. 16 and resembles a center mode in a trans-
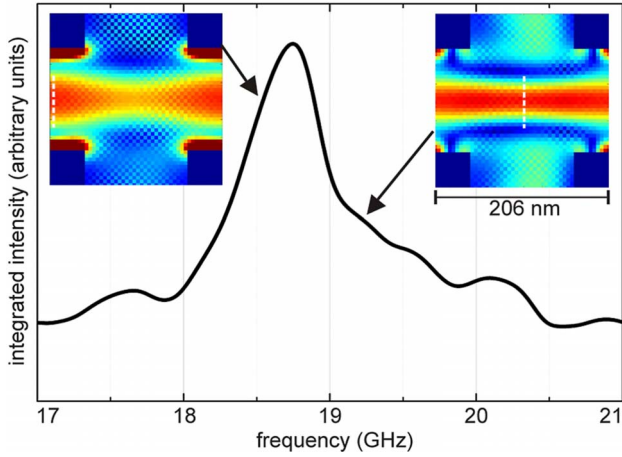
FIG. 4. (Color online) Analysis of excitation 0Deg-2 at 400 mT for lattice 1: FFT of the resonance spectrum around 20 GHz. Insets show simulated spatial mode profiles for different frequencies. For frequencies at the peak and below areas α participate more strongly. This is consistent with experimental observations in Ref. 16.

versely magnetized nanowire which exhibits $k_\perp = 0$. In an antidot lattice, however, the internal field along the horizontal axis is *not* constant, in contrast to the straight wire's case. It is periodically modulated due to the inhomogeneous demagnetization field generated by the holes. Simulations yield a large (small) negative demagnetization field value in area α [cf.Fig. 1(b)] and a small (large) one in area β for high fields / large structures (low fields / small structures). This complex behavior is strikingly different from individual micromagnets and is illustrated in Fig. 1(f) for lattice 3 at different H. Note that at high fields H the periodicity of H_{Dem} equals the lattice constant since the magnetization configuration is a saturated butterfly state. From a detailed Fourier analysis of H_{Dem} in the x and y directions, we find that the Fourier components belong to multiples of the reciprocal lattice constant $2\pi/a$. For small H, however, the periodicity doubles [cf. curve at 60 mT in Fig. 1(f)] since spins in area β deviate significantly from the orientation of $\vec{H}$, whereas spins in area α stay aligned with the external field. As a consequence, a high wave vector of $4\pi/a$ plays a role for momentum transfer through the internal field. This is different from antidot lattices which are assumed to be homogeneously magnetized.

In Figs. 3(a) and 3(i) the displayed modes can be approximated by the center mode of a transversely magnetized nanowire. The vertical magnon wave guides are not excited. For lattice 3, using Eq. (4), setting $k_\perp = 0$, and previously calculating $k_\parallel$ by means of Eq. (1), the semianalytical calculation provides a resonance frequency of 5.53 GHz for mode 0Deg-2 at $\mu_0 H = 60$ mT, in excellent agreement with the simulated eigenfrequency of 5.68 GHz. Testing now the influence of inhomogeneous H_{Dem} (Fourier transform images in Fig. 4), the excitation in the center of the wires becomes more pronounced if one increases H and thereby the eigenfrequency. At 400 mT the *absolute* value of H_{Dem} exhibits a minimum in the area β [Fig. 1(f)] and varies in a sinusoidal manner along the x position. The resonance spectrum exhibits a linewidth of 2 GHz with intensity between 18 to 20 GHz. It is broader than the damping constant would suggest.

Mode profiles for frequencies 18.5 and 19.4 GHz are depicted as insets in Fig. 4. For 18.5 GHz the intensity is highest in area α, and a WKB analysis using Eq. (2) along the broken white line yields $\phi_{\text{WKB}} = 1.13\pi$. For 19.4 GHz the excitation amplitude in the central regions α and β is more homogeneous, and the WKB analysis in area β yields $\phi_{\text{WKB}} = 1.03\pi$. Regions between α and β reach WKB values of π for all frequencies between 18 and 20 GHz. They are not excited due to imaginary wave vectors at lower frequencies. Mode profiles calculated semianalytically all along the y direction are in excellent agreement with simulated results (not shown). Therefore, we attribute the increased linewidth to the influence of the spatially varying demagnetization field, allowing slightly different resonance frequency in different areas along the mode axis, if everywhere $k_\perp = 0$ and $k_\parallel = \text{const}$ is considered. In other words, the prerequisite of a coherent $k_\perp = 0$ leads to a variation of the eigenfrequency along the direction perpendicular to H if the demagnetization field changes within the coherence length of the mode. This explains the spatial mode profile observed in Ref. 16. A similar phenomenon, i.e., partial decoherence, was found by Schultheiss *et al.* in Ref. 34 on microscopic magnetic rings.

We now turn to mode 0Deg-3 in Fig. 3(f). If analyzed by means of our semianalytical approach and Eq. (4), we find that parameters $m=1$, i.e., $k_\parallel = 2\pi/(a-b)$, and $n=0$, i.e., $k_\perp = \pi/a$, give a resonance frequency of 9.39 GHz at 60 mT. This is in good agreement with the simulated mode at 8.95 GHz. Following this analysis, the mode 0Deg-3 in Fig. 3(f) can be understood as an higher-order mode of mode 0Deg-2, which is depicted in Fig. 3(a). In particular, along the y axis it is the asymmetric (cosinusoidal) profile. Indeed, the WKB consistency check based on Eq. (2) yields a value of $\phi_{\text{WKB}} = 2.25\pi$. The mode profile obtained via Eq. (3) is also in excellent agreement with simulation. Setting now $m=0$ and $k_\perp = \pi/a$ and using Eq. (4), one calculates a further eigenfrequency of 7.42 GHz. Within the vicinity of this frequency, we observe no resonance peak in the simulated spectra. Indeed, using Eq. (1) no real wave vectors are found for frequencies in this range, meaning that a mode with $m=0$, i.e., $k_\parallel = \pi/(a-b)$ cannot exist. Similar considerations are valid for the other lattices.

Next, we draw the attention to the fact that the absorption strength of mode 0Deg-2 in lattice 1 becomes weak for decreasing H below $\mu_0 H = 60$ mT, where the eigenfrequeny is at a minimum [Fig. 2(a)]. A similar behavior is observed for lattice 3 in Fig. 2(b), albeit for a slightly lower field of 50 mT. The weakness at small H is attributed to the waterfall magnetization configuration. Decreasing H makes spins rotate to the horizontal direction perpendicular to the external field. This induces a spatially varying x component of M. This causes a change in the mode profile [cf. Fig. 3(g)] and in area β tilts the symmetry axis of the mode away from the y direction, thereby achieving perpendicular alignment to the internal field (not shown). With increasing spin rotation the wave vector $k_\perp = 0$ cannot be realized anymore. In Fig. 3(g) the mode does not extend through the antidot lattice.

3. Localized mode at $\eta = 0°$

We proceed with analysis of mode 0Deg-4, the mode profile of which is depicted in Fig. 3(b) for lattice 3 and in Fig.
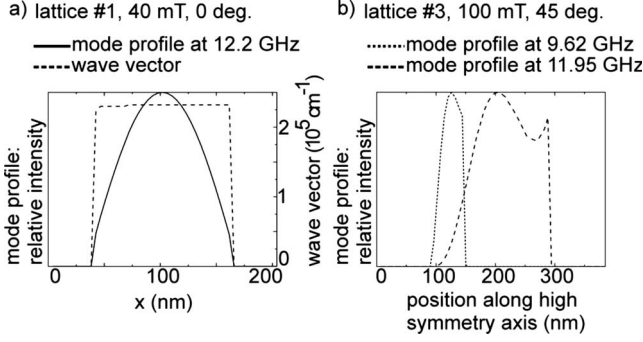
FIG. 5. (a) Mode 0Deg-4 analysis for lattice 1 at 40 mT. The straight line depicts the calculated mode profile using Eq. (3). The dashed line depicts the calculated wave vector $k_\perp$ using $k_\parallel = \pi/b = \pi/85$ nm, where b is the dot diameter. (b) Mode 45Deg-2 analysis (short dashes) and Mode 45Deg-3 analysis (long dashes) for lattice 3 at 100 mT. Only the mode profiles are shown for sake of simplicity.

3(h) for lattice 1. For this mode mainly the vertical magnon wave guides are excited in regions γ. Here, a mode is formed and localized in a potential well, which is caused by strongly varying H_{Dem} [cf. Fig. 1(c)]. We assume a wave vector $k_\parallel = \pi/b$ along the y direction, where b is the dot diameter, i.e., $m=0$. The high symmetry axis is chosen in the x direction in between two adjacent dots, i.e., axis B in Fig. 1. A value of $\phi_{\text{WKB}} = 0.91\pi$ is obtained using Eq. (2). In Fig. 5(a) the results of the mode profile calculation (straight line) based on Eq. (3), as well as the calculated wave vector (dashed line), are depicted. Using Eq. (4) the analysis provides a resonance frequency of 12.88 GHz. Both results are in excellent agreement with the simulations. This is true for the other lattices also.

Interestingly, as can be seen from Fig. 2(a), the pronounced occurrence of mode 0Deg-2 at fields $\gtrsim 60$ mT coincides for lattice 1 with the split up of the high-frequency mode. We find that it splits up into up to four peaks, however only two (0Deg-3 and 0Deg-4) are prominent. Mode patterns are all similar. One such mode at 13.8 GHz is exemplarily depicted in Fig. 3(j). Here, all regions $\alpha, \beta,$ and γ are excited. This pattern can be analyzed in terms of a hybridization of mode profiles illustrated in Figs. 3(h) and 3(i). When we calculate a resonance frequency for a higher order of mode 0Deg-2, using parameters $m=0$ and $n=1$, i.e., $k_\perp = 2\pi/a$, we get 13.89 GHz, a frequency located within the multipeak structure and very close to the mode depicted in Fig. 3(j). The quantized vectors k assumed for the semianalytical calculation reflect the node pattern of Fig. 3(j), albeit the distinct mode profile is not easily reconstructed anymore. We conclude, that even though modes that we discussed so far are separated to a large degree within different areas of the lattice, they can hybridize for a small unit-cell size if eigenfrequencies overlap: we observe such hybridized modes also for lattice 2 and 3, but *not* for lattice 4 with a large lateral size.

4. Extended mode at $\eta = 45°$

We now proceed to analyze modes occurring for $\eta = 45°$. In Fig. 1(h) the magnetization configuration is shown for

lattice 3 at $\mu_0 H = 100$ mT. In Fig. 1(g) the corresponding demagnetization field is depicted. For lattice 3, three prominent modes are extracted from the field dispersion in Fig. 2(c). Lowest in frequency is again the edge mode (45Deg-1) not discussed here for reasons as outlined above. Higher in frequency are modes 45Deg-2 and 45Deg-3. Profiles are depicted in Figs. 3(c) and 3(d) for lattice 3. Mode 45Deg-2 is the *counterpart* of mode 0Deg-2 in the $\eta = 45°$ field alignment. Again the excitation extends throughout the antidot lattice, now in the *diagonal* direction which is perpendicular to $\vec{H}$. We analyze 45Deg-2 by choosing a high-symmetry axis between holes along the external field direction, i.e., along axis C in Fig. 1(b). Assuming $k_\perp = 0$, i.e., a zero wave vector parallel to axis D, the WKB integral of Eq. (2) yields $\phi_{\text{WKB}} = 0.97\pi$. The mode profile calculated semianalytically according to Eq. (3) [Fig. 5(b)] matches very well the simulated one. Importantly, we do not observe extended modes corresponding to 45Deg-2 in lattices 1, 2, and 4. Here, localized edge modes dominate in the respective spatial area. Only for round holes of small diameter, i.e., small inverse filling fraction, we observe the extended mode in the diagonal direction. Therefore, we suggest that the geometry of lattices 1, 2, and 4 consisting of square holes with large diameter does not allow the extended mode 45Deg-2 to form.

5. Localized mode at $\eta = 45°$

We continue the analysis with mode 45Deg-3 occurring at 10.65 GHz [Fig. 3(d)]: Because H_{Dem} varies strongly along axis C of Fig. 1(b), the mode is localized along axis C due to the inhomogeneous field, and the wave vector $k_\parallel$ of this mode changes considerably along this axis. In the orthogonal (axis D) direction the mode is confined between holes. Mode 45Deg-3 is the counterpart of mode 0Deg-4 in the $\eta = 45°$ field alignment. Here, it is instructive to analyze the mode by setting $k_\parallel$ to a value extracted from the simulated mode profile and evaluate $k_\perp$. Doing so for lattice 3 yields a WKB value in Eq. (2) of $\phi_{\text{WKB}} = 0.83\pi$ for $k_\parallel = \frac{\pi}{90 \text{ nm}}$ and a mode profile in good agreement with simulated results. The main outcome of the investigations is that circular holes of lattice 3 with small diameter allow both types of eigenmodes, i.e., extended and localized modes, to form at $\eta = 45°$.

IV. INFLUENCE OF LATTICE SIZE

In this section we compare eigenfrequencies of mode 0Deg-2 (extended modes) for different lateral lattice constants and identify the relevant parameters for the exact spin-wave eigenfrequency. For this we simulated spin-wave dynamics using $\mu_0 H = 400$ mT applied along the y direction ($\eta = 0°$), ensuring the butterfly magnetization state also for the small antidot lattices. The simulated eigenfrequencies are presented as symbols in Fig. 6. They obey a minimum near $(a-b) = 80$ nm. Stimulated by the results of Sec. III B we analytically gain the effective internal field H_{int}, assuming a thin magnetic wire extending parallel to the mode axis in the x direction and having a width of $(a-b)$ [Fig. 1(a)]. To calculate the effective internal field we take the formula given
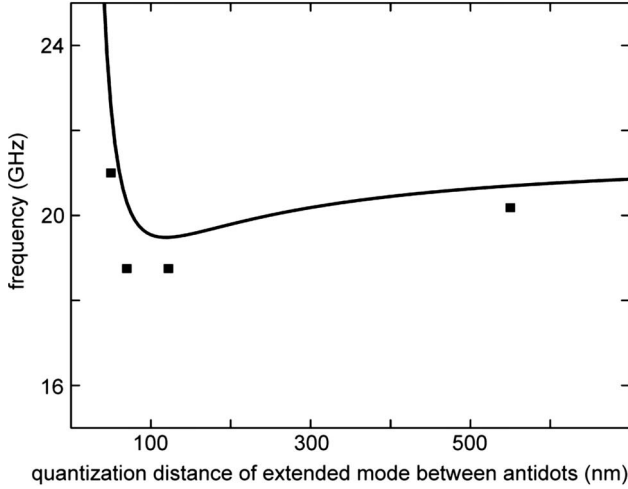
FIG. 6. Eigenfrequency of mode 0Deg-2 at 400 mT as a function of antidot-to-antidot distance (see text). Continuous line is an analytical result using the demagnetization field of a thin wire. Dots are simulated results.

in Ref. 35, a wire length close to infinity, and layer thickness of 24 nm. For sake of simplicity, we assume $k_{\parallel} = \pi/(a-b) \cdot 0.7$. The eigenfrequencies of this analytical approach are presented in Fig. 6 as a continuous line. The simulated eigenfrequencies follow the analytical result. They are systematically smaller. The discrepancy can be attributed to first assuming constant wave vectors in the x and y direction, i.e., $\partial k_{\parallel}/\partial y = \partial k_{\perp}/\partial x = 0$, and second starting from the demagnetization field of an infinitely long wire. The discrepancy is however only a few percent and the analytically calculated curve is still in good agreement with the simulations. Strikingly, for narrow antidot lattices with $(a-b) < 60$ nm the eigenfrequency strongly increases with decreasing $(a-b)$. This is due to the wave-vector quantization and the rapidly increasing vector $k_{\parallel}$. Spin waves are exchange dominated. For increasing distances $(a-b)$ beyond 80 nm the frequency also increases but much slower. In this regime the frequency dependence is due to the dependence of the demagnetization factor on the wire width. Spin-wave modes are dipolar modes. Eventually the eigenfrequency converges, i.e., $\partial \omega/\partial k \approx 0$. As a consequence, the demagnetization field governs the eigenfrequency of mode 0Deg-2 over a very broad regime of lattice constants. We find that mode profiles measured in Ref. 16 on holes with $(a-b) = 1500$ nm and 3500 nm are similar to simulated mode profiles presented in Fig. 3. This consistency can be explained by Fig. 6, where for $(a-b) > 100$ nm the effect of H_{Dem} dominates over the wave-vector quantization. Thus lattices 1—4 and the sample of Ref. 16 fall into the same regime in Fig. 6. The same holds for Ref. 15 with $(a-b) = 150$ nm. Only for very narrow lattices the quantization takes over and determines the eigenfrequency. Fitting a demagnetization field for analysis as suggested in Refs. 14 and 16 becomes inappropriate. Experiments in this regime have not been performed yet.

V. FIELD-CONTROLLED PROPAGATION OF SPIN WAVES

Finally, we investigate how spin waves propagate through an antidot lattice, which is subject to an in-plane magnetic
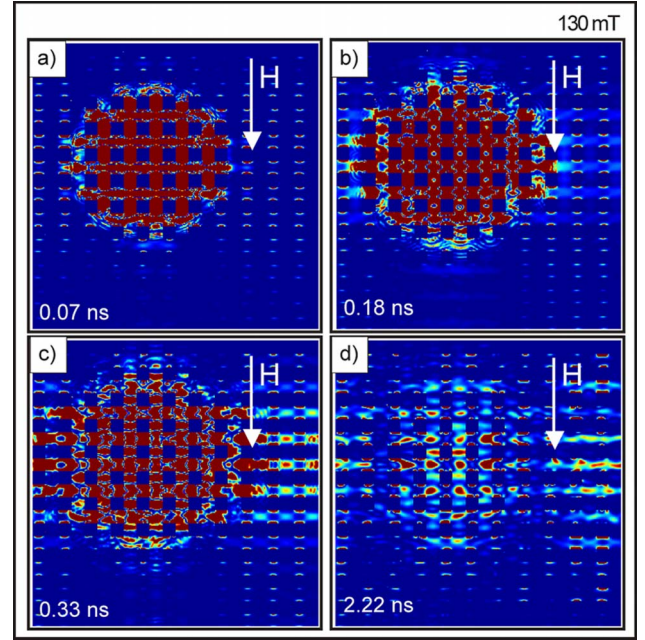

FIG. 7. (Color online) Spin-wave propagation within an antidot lattice: simulated patterns show the time evolution after a pulsed excitation for $\mu_0 H = 130$ mT with a spatial inhomogeneous magnetic field $h(t)$ at (a) 70 ps, (b) 180 ps, (c) 330 ps, and (d) 2200 ps after the field pulse. In the x and y direction eleven unit cells are depicted. Red (bright) represents a high spin-wave amplitude. For long times, i.e., (d), the damping has reduced the overall amplitude. The propagation is predominantly perpendicular to $\vec{H}$, which is applied along the y direction.

field $\vec{H}$. For this we excite the antidot lattice only in a small region by means of a spatially inhomogeneous magnetic-field pulse $\vec{h}(t)$ and analyze the time evolution across the lattice (in contrast to the frequency domain analysis of a single unit cell presented above). $\vec{h}$ points along the x direction. Due to the spatially varying demagnetization field, as well as by the nonuniform excitation, spin waves with a broad range of wave vectors $\vec{k}$ are excited. From Fig. 7 we find that the spin excitation propagates fast in the horizontal x direction, which is perpendicular to the applied magnetic field. In the y direction spin-wave propagation is *suppressed*. We attribute this behavior to the findings in III B. There, vertical magnon wave guides (i.e., wave guides collinear with $\vec{H}$) were found to be excited only locally, i.e., spin waves were localized in potential wells (cf. mode 0Deg-4). In the x direction the extended eigenmode 0Deg-2 built up over many unit cells. This was possible since H_{Dem} varied smoothly along this axis and modes were not localized in potential wells. In the view of propagating spin waves, this scenario provokes the preferential propagation in the x direction seen in Fig. 7. Spin waves are guided in a direction perpendicular to $\vec{H}$. Note that by tilting the field by 45°, we expect the propagation to be pronounced in the diagonal direction [cf. Fig. 3(c)].

For comparison we have studied spin-wave propagation also in an unpatterned $Ni_{80}Fe_{20}$ film subject to $\vec{H}$ pointing

along the y direction (not shown). Here, the pulsed excitation $\vec{h}(t)$ generates propagating spin waves, which exhibit an anisotropic behavior due to different group velocities $\partial\omega/\partial k$ in different spatial directions. A detailed analysis and comparison with Fig. 7 show that the patterning with holes enhances the anisotropic behavior. Thus, both the guiding along the x direction and suppression along the y direction found in Fig. 7 substantiate the characteristic spin-wave modes of the antidot lattice, i.e., extended vs localized modes, respectively. The local potential wells, which we found in the antidot lattice in Sec. III B, inhibit spin-wave propagation parallel to the field. This phenomenon is different from Bragg reflection, where the periodicity of the lattice is decisive.

As a result, magnonic crystals offer further control over wave propagation phenomena due to the inhomogeneous internal field H_{int}. This control goes beyond photonic crystals. Since H_{int} is tailored by the applied field H spin waves are guided by an external means.

VI. CONCLUSIONS

Micromagnetic simulations have allowed us to identify major spin-wave modes in antidot lattices in an applied magnetic field. One type of mode in particular is extending throughout the lattice perpendicular to the external field. Other modes are confined between neighboring dots and localized via the inhomogeneous internal field. These two types have been found also for a magnetic field applied along a diagonal direction. A semianalytical approach has provided the wave-vector quantization conditions. We discuss the impact of the demagnetization field as a function of lattice parameters on mode eigenfrequencies. A significant increase in the eigenfrequency of extended modes is predicted for small antidot lattice unit cells. Furthermore, we have shown that spin-wave propagation perpendicular to the field is favored.

*grundler@ph.tum.de

[1] J. Jorzick, S. O. Demokritov, B. Hillebrands, M. Bailleul, C. Fermon, K. Y. Guslienko, A. N. Slavin, D. V. Berkov, and N. L. Gorn, Phys. Rev. Lett. **88**, 047204 (2002).

[2] S. Choi, K.-S. Lee, K. Y. Guslienko, and S.-K. Kim, Phys. Rev. Lett. **98**, 087205 (2007).

[3] V. V. Kruglyak and R. J. Hicken, J. Magn. Magn. Mater. **306**, 191 (2006).

[4] D. S. Deng, X. F. Jin, and R. Tao, Phys. Rev. B **66**, 104435 (2002).

[5] R. Hertel, W. Wulfhekel, and J. Kirschner, Phys. Rev. Lett. **93**, 257202 (2004).

[6] M. Krawczyk and H. Puszkarski, J. Appl. Phys. **100**, 073905 (2006).

[7] A. Khitun, D. E. Nikonov, M. Bao, K. Galatsis, and K. L. Wang, Nanotechnology **18**, 465202 (2007).

[8] L. J. Heyderman et al., Phys. Rev. B **73**, 214429 (2006).

[9] L. Torres, L. Lopez-Diaz, and J. Iniguez, Appl. Phys. Lett. **73**, 3766 (1998).

[10] C. C. Wang, A. O. Adeyeye, and N. Singh, Nanotechnology **17**, 1629 (2006).

[11] C. Yu, M. J. Pechan, W. A. Burgei, and G. J. Mankey, J. Appl. Phys. **95**, 6648 (2004).

[12] M. Yu, L. Malkinski, L. Spinu, W. Zhou, and S. Whittenburg, J. Appl. Phys. **101**, 09F501 (2007).

[13] O. N. Martyanov, V. F. Yudanov, R. N. Lee, S. A. Nepijko, H. J. Elmers, R. Hertel, C. M. Schneider, and G. Schönhense, Phys. Rev. B **75**, 174429 (2007).

[14] S. McPhail, C. M. Gürtler, J. M. Shilton, N. J. Curson, and J. A. C. Bland, Phys. Rev. B **72**, 094414 (2005).

[15] M. Kostylev, G. Gubbiotti, G. Carlotti, G. Socino, S. Tacchi, C. Wang, N. Singh, A. O. Adeyeye, and R. L. Stamps, J. Appl. Phys. **103**, 07C507 (2008).

[16] M. J. Pechan, C. Yu, R. L. Compton, J. P. Park, and P. A. Crowell, J. Appl. Phys. **97**, 10J903 (2005).

[17] J. Joannopoulos, P. Villeneuve, and S. Fan, Solid State Commun. **102**, 165 (1997).

[18] S. L. Vysotskii, S. A. Nikitov, and Y. A. Filimonov, J. Exp. Theor. Phys. **101**, 547 (2005).

[19] Excitation of mesoscopic magnets with a uniform microwave field gives rise to finite wave-vector momentum transfer via (i) static and dynamic pinning of spins at the geometrical edges (Ref. 29), (ii) an inhomogeneous internal field (Ref. 21), and (iii) reciprocal lattice vectors if a periodic array of magnets is considered (Ref. 36).

[20] F. Giesen, J. Podbielski, T. Korn, and D. Grundler, J. Appl. Phys. **97**, 10A712 (2005).

[21] J. Podbielski, F. Giesen, and D. Grundler, Phys. Rev. Lett. **96**, 167207 (2006).

[22] K. Y. Guslienko, R. W. Chantrell, and A. N. Slavin, Phys. Rev. B **68**, 024422 (2003).

[23] F. Giesen, J. Podbielski, and D. Grundler, Phys. Rev. B **76**, 014431 (2007).

[24] D. Berkov and N. Gorn, Micromagus package for micromagnetic simulations, http://www.micromagus.de

[25] J. Podbielski, D. Heitmann, and D. Grundler, Phys. Rev. Lett. **99**, 207202 (2007).

[26] I. Neudecker, M. Kläui, K. Perzlmaier, D. Backes, L. J. Heyderman, C. A. F. Vaz, J. A. C. Bland, U. Rüdiger, and C. H. Back, Phys. Rev. Lett. **96**, 057207 (2006).

[27] C. Bayer, S. O. Demokritov, B. Hillebrands, and A. N. Slavin, Appl. Phys. Lett. **82**, 607 (2003).

[28] C. Bayer et al., Phys. Rev. B **72**, 064427 (2005).

[29] K. Y. Guslienko, S. O. Demokritov, B. Hillebrands, and A. N. Slavin, Phys. Rev. B **66**, 132402 (2002).

[30] K. Perzlmaier, G. Woltersdorf, and C. H. Back, Phys. Rev. B **77**,

054425 (2008).

[31] M. Bailleul, D. Olligs, and C. Fermon, Phys. Rev. Lett. **91**, 137204 (2003).

[32] As H_{Dem} varies strongly and takes many different values at the edges, forced precession can occur near the holes at eigenfrequencies corresponding to center modes. This is observed in Fig. 3.

[33] We note that the soft mode behavior of mode 0Deg-1, reaching a minimum frequency around $H = 100$ mT for lattice 1, is due to the large and negative demagnetization field value at the outer edge of a hole. We find $H_{Dem} \approx -100$ mT in Fig. 1(d). For a larger hole diameter, e.g. in lattice 4, $H_{Dem} \ll H$ and as expected one cannot observe a soft mode behavior at high fields.

[34] H. Schultheiss, S. Schäfer, P. Candeloro, B. Leven, B. Hillebrands, and A. N. Slavin, Phys. Rev. Lett. **100**, 047204 (2008).

[35] A. Aharoni, J. Appl. Phys. **83**, 3432 (1998).

[36] G. Gubbiotti, S. Tacchi, G. Carlotti, P. Vavassori, N. Singh, S. Goolaup, A. O. Adeyeye, A. Stashkevich, and M. Kostylev, Phys. Rev. B **72**, 224413 (2005).